Title

The relation between microdosimetry and induction of direct damage to DNA by alpha particles

Permalink

https://escholarship.org/uc/item/8629v1gq

Journal

Physics in Medicine and Biology, 66(15)

ISSN

0031-9155

Authors

Bertolet, Alejandro
Ramos-Méndez, José
Paganetti, Harald
et al.

Publication Date

2021-08-07

DOI

10.1088/1361-6560/ac15a5

Peer reviewed

The relation between microdosimetry and induction of direct damage to DNA by alpha particles

Alejandro Bertolet[1], **José Ramos-Méndez**[2], **Harald Paganetti**[1], **Jan Schuemann**[1]

[1]Department of Radiation Oncology, Massachusetts General Hospital and Harvard Medical School, United States of America

[2]Department of Radiation Oncology, University of California San Francisco, United States of America

Abstract

In radiopharmaceutical treatments α-particles are employed to treat tumor cells. However, the mechanism that drives the biological effect induced is not well known. Being ionizing radiation, α-particles can affect biological organisms by producing damage to the DNA, either directly or indirectly. Following the principle that microdosimetry theory accounts for the stochastic way in which radiation deposits energy in sub-cellular sized volumes via physical collisions, we postulate that microdosimetry represents a reasonable framework to characterize the statistical nature of direct damage induction by α-particles to DNA. We used the TOPAS-nBio Monte Carlo package to simulate direct damage produced by monoenergetic alpha particles to different DNA structures. In separate simulations, we obtained the frequency-mean lineal energy (y_F) and dose-mean lineal energy (y_D) of microdosimetric distributions sampled with spherical sites of different sizes. The total number of DNA strand breaks, double strand breaks (DSBs) and complex strand breaks per track were quantified and presented as a function of either y_F or y_D. The probability of interaction between a track and the DNA depends on how the base pairs are compacted. To characterize this variability on compactness, spherical sites of different size were used to match these probabilities of interaction, correlating the size-dependent specific energy (z) with the damage induced. The total number of DNA strand breaks per track was found to linearly correlate with y_F and z_F when using what we defined an effective volume as microdosimetric site, while the yield of DSB per unit dose linearly correlated with y_D or z_D, being larger for compacted than for unfolded DNA structures. The yield of complex breaks per unit dose exhibited a quadratic behavior with respect to y_D and a greater difference among DNA compactness levels. Microdosimetric quantities correlate with the direct damage imparted on DNA.

Keywords

microdosimetry; alpha particles; DNA direct damage; TOPAS-nBio; TOPAS

jschuemann@mgh.harvard.edu .

Introduction

Effects of ionizing radiation on living organisms are mainly driven by the damage induced to the DNA. In particular, double strand breaks (DSBs) of the DNA double helix have been shown to correlate with cell survival after exposition to radiation (Prise *et al* 1987, Ward 1990). After the initial induction of DSBs from radiation effects, mechanisms for DSB detection and repair take place, leading the cell to one of several potential fates depending on the repair success, including loss of ability to proliferate or cell death (Mladenov *et al* 2016). It is also believed that damage complexity, i.e. the formation of clusters of multiple DSBs, plays a major role in the cell's ability to correctly repair damage (Olive 1998, Lorat *et al* 2016). Damage complexity after an irradiation is influenced by the radiation quality, as high linear energy transfer (LET) radiations, such as alpha particles or heavier ions, tend to locally concentrate their energy depositions along their pathway in tissue (Stewart *et al* 2011, Oeck *et al* 2018). This is of particular importance for alpha particle radiopharmaceutical therapy (α-RPT), in which cancer cells are targeted with pharmaceuticals (Guerra Liberal *et al* 2020) that emit low energy (and thus high LET) alpha particles.

Therefore, to adequately predict the outcomes of radiation-driven treatments, it becomes relevant to firstly, quantify the damage induced to DNA and its complexity after a given absorbed dose; and secondly, characterize the repair events happening after the initial induction of damage. For the former, Monte Carlo (MC) simulations are a powerful tool, as the physical and chemical interactions between radiation particles and DNA structures are available in packages such as Geant4-DNA (Incerti *et al* 2010, Karamitros *et al* 2011) or TOPAS-nBio (McNamara *et al* 2017, Ramos-Méndez *et al* 2018, Schuemann *et al* 2019). For the latter, mechanistic models for repair after initial damage induction have been derived (Belov *et al* 2015, McMahon *et al* 2016, Warmenhoven *et al* 2020), taking into account different specific mechanisms and variable radiosensitivity between cell lines exposed to radiation. More empirical models for cell survival, such as the local effect model (Friedrich *et al* 2012) or the microdosimetric kinetic model (MKM) (Hawkins 1996), condense initial damage and repair in a single step, utilizing at the same time biological and radiation biology parameters. In particular, MKM is based on the microdosimetry theory (Kellerer 1985), which accounts for the stochastic patterns of energy deposition from a given radiation. However, although these models offer practical calculations, they mix physical and biological properties, limiting their applicability across different biological systems.

Although the initial energy deposition from physical interactions between radiation and biological matter is the seed for subsequent effects, from a formal point of view microdosimetry only accounts for the energy directly deposited by the considered particles, which gives rise to direct damage to DNA. Therefore, indirect damages induced through chemical and biological processes may follow different, nonlinear proportionalities to microdosimetry as direct effects. Nonetheless, microdosimetry may still represent an excellent tool to predict the dependence of induced DNA damage on the radiation quality, providing a faster way of calculating damage induction than dedicated MC simulations as microdosimetric quantities can be calculated analytically (Bertolet *et al* 2019b, 2020). Thus, a microdosimetric approach could be used for treatment planning in α-RPT. Previous works

have studied the link between the microdosimetric description of track structure and damage induced to DNA by neutrons (Baiocco *et al* 2016), electrons and protons (Hong *et al* 2013). To the best of our knowledge, this is the first study explicitly relating microdosimetry and damage to DNA for alpha particles.

In this work, we used the capabilities of the MC package TOPAS (Perl *et al* 2012, Faddegon *et al* 2020) to calculate the microdosimetric properties of monoenergetic alpha particles, extending our previous studies (Bertolet *et al* 2020). Then, we employed the TOPAS-nBio extension (Schuemann *et al* 2019) to characterize the direct damage to DNA produced by the same alpha particles, using several different DNA structures available in this extension. This work aims at finding correlations between microdosimetric quantities and initial direct damages induced in DNA by alpha particles.

Methods and materials

Simulations with DNA structures in TOPAS-nBio

To characterize the damage that monoenergetic alpha particles inflict on the DNA, we performed simulations of DNA damage induction in TOPAS-nBio, using different ways for DNA to fold. In particular, we considered: (a) DNA helices in straight lines and arranged in hexagonal packing as in λ phage DNA (Hud and Downing 2001), so-called linear plasmids; (b) supercoiled plasmids representing the pBR322 *E. coli* cloning vectors folded following two different paths labeled as 'A' and 'B' (McNamara *et al* 2018); and (c) solenoid chromatin fibers, in which the double helix is wrapped around a cylindrical histone protein as in a typical cell nucleus (Zhu *et al* 2020). For all geometries, DNA backbones and bases were modeled as spheres of radius equal to 0.29 nm and 0.208 nm, respectively, and the distance between each base pair was 0.34 nm. Due to limitations in available cross sections at very low energies, all DNA structures were embedded in a liquid water medium and were considered to be made of liquid water as well. For the solenoid geometry, histones were modeled as cylinders of 3.3 nm radius and 5.7 nm length, whereas the entire solenoid has a radius of 19.04 nm.

In order to avoid burdensome simulations involving billions of base pairs, we employed more efficient geometries in which replicated plasmids of each one of the four DNA configurations were arranged inside micrometric spheres. Specifically, 1286 base pair long linear plasmids were arranged in a 250 nm radius sphere in parallel forming a hexagonal prism, with rows and columns both separated by 2.8 nm as shown in figure 1(a). This setup includes 4.403 mega base-paris (Mbp) in the considered volume. We performed two different simulations with supercoiled plasmids, using two types of paths for the double helix, shown in figure 1(b). Simulations with supercoiled plasmids using the path 'A' were done by replicating them in voxels of 52.75 nm × 68.47 nm × 175.43 nm, while simulations with supercoiled plasmids 'B' used voxels of 81.49 nm × 92.08 nm × 202.46 nm. To ensure the same order of magnitude of DNA material in our simulations, which may be relevant from a statistical point of view, spheres with radius of 500 nm were used as containers, so that 189 plasmids 'A' (0.83 Mbp) and 35 plasmids 'B' (0.15 Mbp) were contained, respectively. Finally, figure 1(c) shows the arrangement for the 288 nm long solenoid fibers. 49 fibers were placed in a 250 nm radius sphere in parallel in a rectangular pattern, with

rows and columns of cylinder axes each 38 nm. Each fiber contained 23.5 kbp, so 1.15 Mbp were included overall. The sphere surface, in each case, was employed as an isotropic source of monoenergetic alpha particles so that results were averaged out throughout all possible orientations between the DNA arrangements and the particle track. Alpha particles were simulated with initial kinetic energies of 1, 2, 3, 5 and 10 MeV for each case, as typically alpha particle emissions in α-RPT are not greater than 10 MeV. The default physics list of TOPAS-nBio for Geant4-DNA (Incerti *et al* 2010, 2018) was employed for all simulations.

A DNA strand break was considered to happen when 17.5 eV or more energy was deposited into a base or a backbone. DBSs were defined as two breaks occurring at complementary strands at a distance of at most 10 base pairs. All breaks not paired with another break on the other strand within 10 base pairs were classified as single strand breaks (SSBs). Complex breaks (CBs) were defined as the accumulation of one DSBs and either one or more SSBs or one or more DSBs within 10 base pairs, i.e. the maximum extent of a CB is 10 bp. While DSBs and SSBs were exclusive, i.e. a DSBs is not counted as two SSBs, CBs scoring was independent: those DSBs present in a CB were still counted as individual DSBs. Figure 2 illustrates the classification of types of damage used in this work.

We scored the total number of breaks B_i, as well as the number of SSBs, DSBs and CBs produced per alpha particle track i of each energy on each DNA arrangement. The longer the track in a volume of DNA, the larger the number of breaks for a given simulation. To account for the track length dependence, we also scored the length of the ith particle track inside the sub-volume that contains DNA, $l_{DNA,i}$. As the DNA does not completely fill the sub-volume, i.e. there is some void space without DNA, not every incident track interacts with a DNA base pair. Also, the number of interactions occurring for a given track will depend on the void along the track trajectory with length $l_{DNA,i}$ which in turn varies for each DNA arrangement considered. A way to address this issue is to consider the *mass* track length, defined in Gbp nm^{-2} as $\rho_{DNA}\bar{l}_{DNA}$, where $\rho_{DNA} = N_{bp}/V_{DNA}$ is the volumetric density of base pairs and $\bar{l}_{DNA} = \sum l_{DNA,i}/N$ is the mean track length after N tracks. In this sense, the number of damages induced by a given particle will be proportional to the mass track length of that particle in a given DNA arrangement. However, note that the mass track length does not account for the tracks only traveling through void space, but it represents a measure of the mean number of interactions a particle will undergo within the DNA volume. Let f be the fraction of tracks—or fluence—that interact with the DNA contained in it. Then the quantity

$$B_{\Phi}\left[\frac{\text{nm}^2}{\text{Gbp}}\right] = f\left[\frac{\sum_{i=1}^{N} B_i/N}{\rho_{DNA}\sum_{i=1}^{N} l_{DNA,i}/N}\right] = f B'\left[\frac{\text{nm}^2}{\text{Gbp}}\right] \tag{1}$$

represents the total number of breaks per giga base pair (Gbp) produced per unit fluence Φ incident into each geometry while $B' = \left(\sum_{i=1}^{N} B_i\right)/\left(\rho_{DNA}\sum_{i=1}^{N} l_{DNA,i}\right)$ represents the number of breaks per mass track length, i.e. per Gbp and unit fluence when all tracks interact with DNA. In what follows, note that B_{Φ} and B' can be substituted by SSB_{Φ}, DSB_{Φ} or CB_{Φ}, and SSB', DSB' or CB', i.e. the number of SSBs, DSBs and CBs per base pair in total and per interacting track, respectively. Therefore, in general, the number of breaks

induced by a given fluence into a given DNA arrangement is proportional to the quotient of the mass track length of the particles composing the fluence and the fraction f of interacting fluence.

Similarly, if the dose absorbed per unit planar fluence in the volume in which DNA is contained, D/Φ, is known, the yield of total breaks Y_B (and Y_{SSB}, Y_{DSB} and Y_{CB}) can be obtained as

$$Y_B \left[\frac{1}{\text{Gy Gbp}} \right] = \left(\frac{\Phi}{D} \right) f B' \left[\frac{\text{nm}^2}{\text{Gbp}} \right]. \qquad (2)$$

The fraction of interacting particles f is obtained with respect to the particles directly impinging on the sub-volume filled with DNA in each case and depends strongly on the way in which DNA is coiled or condensed. In this fraction we also considered secondary electrons from tracks external to V_{DNA} that enter the volume and interact with the DNA. Therefore, it is possible to have a fraction greater than one if there are more interacting external tracks than non-interacting internal tracks. In general, one can think of this fraction as the ratio between an effective irradiated area σ_{eff} to the actual area σ over which the fluence is distributed. When considering a given volume being irradiated, the tracks are distributed across the two-dimensional projection of this volume. If a sphere is considered, then this projection is a circle of area $\sigma = \pi r^2$. An effective spherical volume V_{eff} can be associated to each fraction f using

$$r_{eff} = \sqrt{\frac{f\sigma}{\pi}}. \qquad (3)$$

Equation (3) provides thus a relation between the effective volume and the probability of interaction, expressed in terms of the fraction of interacting tracks f. Note that this effective volume is a virtual concept resembling a relative indicator of the probability for a track to interact with the DNA contained in the actual volume. Therefore, r_{eff} is a parameter without physical meaning to allow relative comparison across different DNA geometries. Consequently, its absolute value requires an arbitrary election of the effective volume associated to $f = 1$. The utility of this description lies on the direct connection with the concept of site in microdosimetry: spherical effective volumes can be associated to spherical sites. In this sense, we have selected a typical site dimension in microdosimetry—$r_{eff} = 500$ nm—as the arbitrary reference value for which $f = 1$ by definition. This is illustrated in figure 3.

The connection of the concept of effective volume with microdosimetry

As mentioned above, the use of a representative spherical volume V_{eff} is convenient because it can be naturally related to the concept of site in microdosimetry. A site represents the volume in which patterns of energy deposition are accounted for (Bertolet *et al* 2019b). Two quantities of interest in microdosimetry are considered in this work. On the one hand, specific energy (z) is the energy imparted into the site per unit mass including those interactions between both the primary charged particles and the secondary electrons

generated along their way. If the specific energy imparted by each single track—including all the secondary particles—z_1 (single-event distribution) is considered, one can average the z_1 values depending upon the frequency of appearance of each value (z_F) or the dose imparted by each track (z_D). As z_F represents the mean specific energy (i.e. dose) imparted by a single particle, it is possible to estimate the dose that a uniform circular fluence composed of N particles, i.e. $\Phi = N/\pi r^2$, imparts to a site of radius r:

$$D' = N z_F = \Phi \pi r^2 z_F \qquad (4)$$

so that the dose for a fluence composed of one single track is given by z_F. The notation D' accounts for the fact that this relation disregards the contribution to the dose from secondary electrons originated by tracks in the vicinity of the site instead of directly traversing it. The product $\pi r^2 z_F$ is expected to be the same for any site as long as the site dimension is much larger than the range of secondary electrons, i.e. the typical width of the alpha particle track. On the other hand, lineal energy (y) is the energy imparted by a single particle track into a given volume-site-divided by the mean chord length ($\bar{l}$) in the site (Bertolet $et\ al$ 2019a). Similarly, it can be averaged depending on frequency (y_F) or dose (y_D). Interestingly, as the mean energy imparted by a track roughly increases linearly with the length of the track in the site, y_D can be considered to be approximately independent of the site size (Newpower $et\ al$ 2019, Bertolet $et\ al$ 2021). This condition breaks again when many secondary electrons escape the site, i.e. when the track width is in the order of the site dimensions or when the site becomes too large and the primary particle loses too much energy. Note that the relation between averages of z and y is trivial for spherical sites as long as the site radius r and density ρ are known: $z_D = y_D/\rho \pi r^2$ (the same relation holds for the frequency-mean quantities).

Microdosimetry simulations and model

To establish the averages of the specific energy imparted by alpha particles to different site volumes, and to investigate the limit of the assumptions of constancy for y_D and $\pi r^2 z_F$, we performed simulations for monoenergetic alpha particles in spherical sites with radius ranging from 50 to 375 nm. For these simulations, a fixed track was placed in a box of liquid water and the lateral position of the spherical site was uniformly sampled. The maximum distance from the center was equal to the maximum range of the secondary electrons produced by alpha particles in water, estimated according to the Tabata's formula (Tabata $et\ al$ 1972), which ranges from 44 nm for 1 MeV to 836 nm for 10 MeV α-particles, respectively. An upstream margin equal to this maximum range of secondary electrons of liquid water to ensure electronic equilibrium in the site was also added, so that the site position along the track was fixed. The default physics list in TOPAS-nBio v1.0 for Geant4-DNA was used in the whole box of liquid water. More details can be found elsewhere (Bertolet $et\ al$ 2019a, 2019b, 2020).

As previously shown (Bertolet $et\ al$ 2019b, 2020), microdosimetric average quantities—i.e. y_F, y_D, z_F and z_D—can be analytically calculated using specific kinetic energy-dependent functions for the average of the distribution of energy imparted to a given site of radius r_s

$$\bar{\varepsilon}(E) = C_s \cdot \text{erf}\left(k_s E^{q_s}\right) \cdot \log\left(7.017\,E + b_s\right) \cdot \frac{1.946\,E^{0.752} + e_s}{1.946\,E^{1.752} + 4r_s/3} \tag{5}$$

and this standard deviation of this distribution

$$\sigma_{\varepsilon}(E) = C_s' \cdot \text{erf}\left(k_s' E^{q_s'}\right) \cdot \log\left(7.017\,E + b_s'\right) \cdot \frac{1.946\,E^{0.752 - f_s'} + e_s'}{1.946\,E^{1.752} + 4r_s/3}. \tag{6}$$

Parameters C_s, k_s, q_s, b_s and e_s in equation (5) (and their corresponding primed versions in equation (6)) depend on the site size and can be obtained by fitting the expressions to the results for mean and standard deviation of energy imparted in MC simulations. In a previous work (Bertolet *et al* 2020), we obtained these parameters for sites with radius of 500, 2500 and 5000 nm. In this work, we obtained the values of these parameters for a 250 nm radius site in order to extend the applicability of our previous results towards smaller sites.

Calculation of results from monoenergetic to polyenergetic beams

While our results, for both damage to DNA and microdosimetric quantities, are restricted to monoenergetic particles, we have previously shown (Bertolet *et al* 2020) how to obtain general results of microdosimetric quantities, i.e. for polyenergetic beams. In particular, if the spectral fluence of alpha particles $\Phi_E(E)$ is known, then the frequency-mean lineal energy for the polyenergetic beam results from weighting each monoenergetic $y_F(E)$ by the number of particles of that energy in the spectrum:

$$y_F = \int \Phi_E(E)\, y_F(E)\, \mathrm{d}E \tag{7}$$

and the dose-mean lineal energy of the polyenergetic beam is the result of weighting each monoenergetic $y_D(E)$ by the dose $D(\Phi_E(E))$ imparted by the particles of energy E:

$$y_D = \int D(\Phi_E(E))\, y_D(E)\, \mathrm{d}E. \tag{8}$$

The same applies to z_F and z_D, respectively. Similarly, B_Φ, the number of breaks per unit fluence incident, for a polyenergetic beam will be given by the breaks produced by each monoenergetic component weighted by its relative frequency (number of tracks) in the spectrum, i.e.:

$$B_\Phi = \int \Phi_E(E)\, B_\Phi(E)\, \mathrm{d}E. \tag{9}$$

Finally, the yield of breaks produced by a polyenergetic beam is the dose-weighted average of the yield $Y_B(E)$ produced by monoenergetic beams:

$$Y_B = \int D(\Phi_E(E)) \, Y_B(E) \, \mathrm{d}E .$$

(10)

Therefore, when dealing with polyenergetic beams, B_Φ is averaged out in the same way y_F is, while Y_B is averaged similar to y_D. It is then convenient to relate these quantities with each other even for monoenergetic cases.

Calculation of results for mixed DNA structures

In the range of site sizes in which the lineal energy distribution can be considered approximately constant, the averages of y only depend on the radiation quality and do not consider any volumetric effect. Therefore, it is not possible from the single use of y to characterize the fraction of particles interacting with DNA. However, through the concept of effective volume, z adds information about the effective volume for a particle to interact, providing the probability of interaction through equation (3). This makes it possible to use z-based results to estimate the results for a combination of different DNA elementary structures. For instance, if two geometries have mixed DNA content equal to N_{bp1} and N_{bp2}, respectively, the specific energy (either z_F or z_D) of the mixed geometry z_{mix} for a given fluence of alpha particles can be related to the specific energies of each geometry, z_1 and z_2 by weighting each one by the inverse of the number of base pairs:

$$z_{mix} = \frac{\dfrac{z_1}{N_{bp1}} + \dfrac{z_2}{N_{bp2}}}{\dfrac{1}{N_{bp1}} + \dfrac{1}{N_{bp2}}} .$$

(11)

For the presented cases, z_1 and z_2 are calculated using the effective radius corresponding to each geometry. To corroborate equation (11), we performed similar simulations mixing solenoid chromatin fibers (as in figure 1(c)) with (a) supercoiled plasmids 'A', having 0.43 Mbp of supercoiled DNA and 1.34 Mbp of chromatin fibers; and (b) supercoiled plasmids 'B', having 78.4 kbp of supercoiled DNA and 0.274 Mbp of chromatin fibers. For these simulations, the rectangular boxes for supercoiled plasmids used in figure 1 were taken and half of the supercoiled plasmids were replaced by chromatin fibers in an alternate way.

Results

Microdosimetric simulations

Figure 4(a) shows the results for y_D from TOPAS simulations of monoenergetic alpha particles from 1 to 10 MeV for different site sizes. This determines the site size limit for which the dose-mean lineal energy can be considered as constant. We also fitted equations (5) and (6) to the results for the 500 nm radius site and compared the y_D calculated using the analytical model with simulations. Figure 4(b) shows a map of the relative variations in y_D as a twofold function of energy and site size with the site of 500 nm as radius set as reference. Agreement with the reference is gradually represented by dark to pale areas in the shown energy-site radius map. Areas between energy-site radius points simulated were

obtained by cubic spline interpolation of the results. Figure 4(c) depicts the dependence of the product $\pi r^2 z_F$ on the site size for different particle kinetic energies. These results show that both y_D and $\pi r^2 z_F$ tend to diverge when decreasing the site size. In particular, the 5% agreement with the analytical y_D for 500 nm radius site is lost for radii below 100 nm and increasing energies. The curves $\pi r^2 z_F$ against site radius tend to reach a plateau, with variations lower than 4% for site radii greater than 300 nm in all energies shown.

Damage to different DNA structures

Total breaks B_Φ obtained per unit fluence and Gbp for the four DNA arrangements in TOPAS-nBio are shown in figure 5(a) as a function of y_F—obtained using the microdosimetric simulations in TOPAS for a site with radius of 500 nm. Figure 5(b) shows the fraction f of interacting tracks for each case and the corresponding effective radius r_{eff} using equation (3). A decrease in f can be observed as the energy decreases due to the shorter range of the secondary electrons, which in turn makes the track narrower and thus decreases the probability of interaction. Breaks per track and Gbp were approximately linear with respect to y_F and essentially the same for all geometries, with the exception of the 1 MeV alpha particles ($y_F = 212$ keV μm^{-1}) for supercoiled plasmids. For that case, the number of breaks was clearly lower than for chromatin fibers and linear plasmids. This effect may be explained by the larger spheres used to contain the supercoiled DNA geometries to contain more DNA, which would imply a significant change in the particle's energy loss inside the sphere. Effective radii depended strongly on the type of DNA geometry and slightly on the kinetic energies (or y_F) of the alpha particles. Mean effective radii were 628 nm for linear plasmids; 517 nm for chromatin fibers; 449 nm for supercoiled plasmids 'A' and 400 nm for supercoiled plasmids 'B'.

To disregard the effects on the induction of complex damage to DNA when comparing among the simulated DNA arrangements, figure 6 shows both the obtained DSB and CB per track and per Gbp together with the ratio between DSB_Φ (and CB_Φ) to B_Φ as a function of y_F. Linear plasmids showed less DSBs and CBs per break than the rest of the geometries, particularly as y_F increases (or, equivalently, energy decreases). DSB_Φ—i.e. absolute number of DSBs per track per Gbp—showed a quadratic relationship with y_F while CB_Φ increases more dramatically with y_F. However, the relative number of DSBs and CBs to the total number of breaks in each case seemed to follow linear and quadratic relationships, respectively.

Using $z_F = y_F / \rho \pi r^2$ and equation (4), we can obtain absorbed dose per unit fluence and obtain the yield of breaks per Gy, Y_B, as well as Y_{DSB} and Y_{CB}. Figure 7 shows the calculated yields of DSBs and CBs for each case as a function of y_D. As it happened with the ratio of DSBs (and CBs) to the total number of breaks, the yield of DSBs can be roughly approximated as linear with respect to y_D, while the yield of CBs increased more sharply with y_D.

Damage per interacting track and relation to effective radius

In equation (1), B' represents the number of breaks produced per mass track length and per Gbp when all tracks in the incident fluence interact with DNA are considered. This is

related to the total number of breaks via the fraction of interacting particles f, which in turn is related to the so-called effective radius r_{eff} through equation (3). Figure 8 shows the number of breaks per track and the yield of DSBs per Gbp if only tracks interacting with the DNA (B' and Y'_{DSB}) are considered. B' and Y'_{DSB} are show with respect to z_F and z_D when using the effective radius r_{eff} as the radius of the microdosimetric site. Both B' and Y'_{DSB} showed an approximately linear trend with respect to z_F and z_D, respectively. Effects of the simulated DNA geometry were more visible for the yield of DSBs than for the total number of breaks. A linear fit for both relationships yielded $B'(z_F) = 59.3 + 24.7$ $z_F (R^2 = 0.995)$ for the total number of breaks per interacting track with respect to z_F and $Y'_{DSB}(z_D) = 0.25 + 0.05 \, z_D \left(R^2 = 0.98 \right)$ for the yield of DSBs per interacting track with respect to z_D. These relationships will be used in the following section.

Prediction of damage to mixed DNA structures

After determining the effective volume for chromatin fibers and supercoiled plasmids, we calculated z using those effective volumes as sites. Then, using equation (11) and results in figure 8, we estimated the corresponding z_F and z_D for mixtures of chromatin fibers and supercoiled plasmids of type 'A' and 'B', respectively. Table 1 shows the calculated $z_{F_{mix}}$ and the $r_{eff_{mix}}$ for each energy. We calculated the corresponding estimated fraction of interaction f using equation (3) as well as B' and Y'_{DSB} from the linear fits to the points in figure 8. We used and f, B' and Y'_{DSB} to calculate the total number of breaks and the yield of DSBs in each geometry-energy combination. Finally, these predictions were compared with results of DNA damage induction obtained when simulating the irradiations of volumes half-filled with chromatin fibers and supercoiled plasmids. Differences between the total number of breaks for the mixtures estimated using our fit method and simulation results did not exceed 7%, while the yield of DSBs showed poorer agreement, with differences up to 13%. Except for 1 MeV alphas, all predictions are within 2σ of the statistical uncertainties of our simulations.

Discussion

We studied the direct damage induced by alpha particles into DNA structures and the relation to microdosimetric properties. The two main results from this work are: (a) there are linear correlations between the number of breaks and the number of DSB induced by alpha particles and the microdosimetric quantities y_F and y_D, respectively; and (b) even when the total number of breaks of DNA strands are equivalent for all DNA structures or compactness, the way in which DNA is coiled has an impact on the complexity of the damage. A possible explanation for the latter is that, intensely coiled DNA plasmids have a smaller cross-sectional area, so that less particles of a uniform fluence interact with DNA. This way, when the same energy is imparted by less tracks, high concentrations of local energy are more likely to happen thus more complex damage is produced. DSBs were computed as individual even when they were clustered in more complex damage to allow comparisons with other studies where total DSB yield is shown (Sakata *et al* 2019, Zhu *et al* 2020). In any case, the relative number of complex DSBs did not exceed 1% for any of the simulations performed in this work.

As shown in figures 5(a) and 7(a), two linear relations are identifiable for all considered DNA structures. First, the total number of breaks *per unit fluence* B_Φ produced by an alpha particle is proportional to its frequency-mean lineal energy y_F. As shown in equations (7) and (9), breaks per track and y_F are obtained for polyenergetic beams by weighting each monochromatic contribution by its component in terms of number of tracks. Therefore, the same linear relationship as shown in figure 5(a) is expected to hold for polyenergetic beams. As also y_F is equal, by definition, to the restricted track averaged LET of a polyenergetic beam, this means that restricted track averaged LET is, at least for alpha particles within the studied energies, proportional to the total number of breaks directly induced to the DNA. Second, the yield of DSBs *per unit dose* Y_{DSB} after an irradiation with alpha particles is proportional to the dose-mean lineal energy y_D. Following similar reasoning and according to equations (8) and (10), this linear relationship still holds for polyenergetic beams. As restricted dose averaged LET is proportional to y_D—differences reside in the variability of energy imparted due to varied chord length and energy straggling—restricted dose averaged LET is, at least for alpha particles within the studied energies, proportional to the number of DSBs directly induced to the DNA. These results provide a novel interpretation of restricted LET averages, which are used in particle therapy to consider the effects of radiation quality.

In particular, our simulations provided approximately the same total number of breaks for any DNA structure from alpha particles of the same energy, which is the expected results when a large number of particles coming from all possible directions is utilized and averaged out. This is the case at least for direct damage, but an equivalent statement for indirect damage needs to be further investigated. An exception is the 1 MeV case for the supercoiled plasmids, for which about 5% fewer total breaks were scored. As already mentioned, this is an effect of the longer path length in these simulations, which utilized spheres with radius of 500 nm instead of 250 nm as for the other two geometries. These distances result in a significant loss of energy for a 1 MeV particle, whose continuous slow-down approximation range is estimated to be about 6 μm. This effect also may play a role in the larger differences observed in table 1 for 1 MeV particles from simulations of mixing supercoiled plasmids and chromatin fibers, as in this case the 500 nm radius sphere is also used. Assuming that a given fluence imparts the same dose in the same volume, the total number of breaks per dose also matches for each energy. These results should be applicable to any other DNA geometry as they represent the average direct damage produced by alpha particles to DNA regardless of geometrical particularities. In fact, our results for direct DSBs are in the same order of magnitude as other references considering only direct damage from alpha particles (Urushibara *et al* 2008, Yokoya *et al* 2008). Nonetheless, absolute results for simulations are conditioned by the geometric models employed for DNA, as direct damage largely depends on the volume of DNA components (Sakata *et al* 2019). However, trends and relations between microdosimetric quantities and production of damage should generally hold.

However, as shown in figures 6(b) and (d), appreciable differences in the complexity of the damage arose between linear and coiled plasmids. These differences increased to about 8% for the ratio of DSBs and total breaks and about 13% for the ratio of CBs and total breaks, i.e. the degree of damage complexity in each case. This also is consistent with some previous literature, showing a greater yield of direct DSBs on highly condensed

DNA than on less condensed DNA (Dos Santos *et al* 2014, Tang *et al* 2019). However, in cases in which not only direct damage is considered, but also indirect damage induced by reactive species from water radiolysis, a greater compactness may induce protection to the inner DNA region which in fact reduces the damages to the DNA (Ljungman 1991, Nygren *et al* 1995, Radulescu *et al* 2004). No clear differential trends are observed between the direct damage to the other three coiled DNA geometries, in part due to the larger uncertainties for the used supercoiled plasmids because of their less organized structure, which is translated into more void space among DNA and, effectively, into lower density of DNA material. Nonetheless, clear differences are seen in our z-based formalism, which uses the number of breaks per mass track length (i.e. fraction of the fluence effectively interacting with DNA), B', instead of per the total fluence $B_\Phi = fB'$. As shown, B' and Y'_{DSB} also follow approximate linear relationships to z_F and z_D when the so-called effective radii are employed as site radius for each geometry. This formulation has the advantage that it implicitly includes the possible differences in damage complexity between DNA structures. Results for combinations of different structures can be obtained as well as shown in table 1. Additionally, the found radii for each structure were, according to figure 4, in a region for which microsimetric quantities (i.e. y_D and $\pi r^2 z_F$) are stable and can be considered constant. This offers an additional advantage to use analytical models based on this formalism, as the dependence on the site size for z can be easily accounted by a factor r^{-2}.

As mentioned in the introduction section, the direct relationship between microdosimetry and direct damage was expected, as the common feature of both is that only physical interactions—and their degree of local concentration—are considered. However, this is only a part of the problem, as indirect damage may represent as much as 80% of the damage even for low energy alpha particles (Tang *et al* 2019). Therefore, indirect damage caused by free radicals produced in chemical reactions needs to be incorporated in order to generate realistic predictions to be used in treatment planning. This represents the next natural step for this work. Here, we showed that microdosimetry naturally links with direct damage to DNA at a first step towards bottom-up treatment planning approaches.

Conclusions

Direct damage to DNA caused by monoenergetic alpha particles can be correlated to microdosimetric quantities. In particular, for direct damage to the DNA, the total number of breaks produced per track correlates to frequency-mean lineal energy (y_F) while the yield of DSBs correlates to dose-mean lineal energy (y_D). In this study we included effects of different DNA geometric arrangements. While the total number of breaks produced by direct damage is the same regardless of DNA compaction, the complexity of the damage was higher for coiled than for stretched DNA strands. This can be attributed to the different probability for a track to interact with the DNA structures in each case, which in turn can be translated into an effective volume representing the interaction probability. When this volume was used as the microdosimetric site, both the total number of breaks per track and the yield of DSBs considering only tracks interacting with DNA showed direct correlations with z_F and z_D, respectively. These correlations provide a useful framework to predict the

direct damage that polyenergetic alpha beams as experienced in radionuclide therapy may produce through microdosimetric quantities.

Acknowledgments

References

Baiocco G et al. 2016 The origin of neutron biological effectiveness as a function of energy Sci. Rep 6 1–14 [PubMed: 28442746]

Belov OV, Krasavin EA, Lyashko MS, Batmunkh M and Sweilam NH 2015 A quantitative model of the major pathways for radiation-induced DNA double-strand break repair J. Theor. Biol 366 115–30 [PubMed: 25261728]

Bertolet A, Baratto-Roldán A, Barbieri S, Baiocco G, Carabe A and Cortés-Giraldo MA 2019a Dose-averaged LET calculation for proton track segments using microdosimetric Monte Carlo simulations Med. Phys 46 4184–92 [PubMed: 31169910]

Bertolet A, Baratto-Roldán A, Cortés-Giraldo MA and Carabe-Fernandez A 2019b Segment-averaged LET concept and analytical calculation from microdosimetric quantities in proton radiation therapy Med. Phys 46 4204–14 [PubMed: 31228264]

Bertolet A, Cortés-Giraldo MA and Carabe-Fernandez A 2020 An analytical microdosimetric model for radioimmunotherapeutic alpha emitters Radiat. Res 194 403–10 [PubMed: 33045091]

Bertolet A, Cortés-Giraldo MA and Carabe-Fernandez A 2021 Implementation of the microdosimetric kinetic model using analytical microdosimetry in a treatment planning system for proton therapy Phys. Medica 81 69–76

Dos Santos M, Clairand I, Gruel G, Barquinero JF, Incerti S and Villagrasa C 2014 Influence of chromatin condensation on the number of direct dsb damages induced by ions studied using a monte carlo code Radiat. Prot. Dosim 161 469–73

Faddegon B, Ramos-Méndez J, Schuemann J, McNamara A, Shin J, Perl J and Paganetti H 2020 The TOPAS tool for particle simulation, a Monte Carlo simulation tool for physics, biology and clinical research Phys. Medica 72 114–21

Friedrich T, Scholz U, Elssser T, Durante M and Scholz M 2012 Calculation of the biological effects of ion beams based on the microscopic spatial damage distribution pattern Int. J. Radiat. Biol 88 103–7 [PubMed: 21823820]

Guerra Liberal FDC, O'Sullivan JM, McMahon SJ and Prise KM 2020 Targeted alpha therapy: current clinical applications Cancer Biother. Radiopharm 35 404–17 [PubMed: 32552031]

Hawkins RB 1996 A microdosimetric-kinetic model of cell death from exposure to ionizing radiation of any LET, with experimental and clinical applications Int. J. Radiat. Biol 69 739–55 [PubMed: 8691026]

Hong Z et al. 2013 Lineal energy-based evaluation of oxidative DNA damage induced by proton beams and x-rays Int. J. Radiat. Biol 89 36–43 [PubMed: 22901337]

Hud NV and Downing KH 2001 Cryoelectron microscopy of λ phage DNA condensates in vitreous ice: the fine structure of DNA toroids Proc. Natl Acad. Sci. USA 98 14925–30 [PubMed: 11734630]

Incerti S et al. 2010 The Geant4-DNA project Int. J. Model. Simul., Sci. Comput 1 157–78

Incerti S et al. 2018 Geant4-DNA example applications for track structure simulations in liquid water: a report from the Geant4-DNA Project Med. Phys 45 e722–39

Karamitros M et al. 2011 Modeling radiation chemistry in the geant4 toolkit prog Nucl. Sci. Technol 2 503–8

Kellerer AM 1985 Fundamentals of Microdosimetry the Dosimetry of Ionization Radiation ed Kase KR et al. vol I (Orlando, FL: Academic) pp 77–162

Ljungman M1991The influence of chromatin structure on the frequency of radiation-induced DNA strand breaks: a study using nuclear and nucleoid monolayersRadiat. Res12658–64 [PubMed: 2020739]

Lorat Y, Timm S, Jakob B, Taucher-Scholz G and Rübe CE 2016 Clustered double-strand breaks in heterochromatin perturb DNA repair after high linear energy transfer irradiation Radiother. Oncol 121 154–61 [PubMed: 27637859]

McMahon SJ, Schuemann J, Paganetti H and Prise KM 2016 Mechanistic modelling of DNA repair and cellular survival following radiation-induced DNA damage Sci. Rep 6 1–14 [PubMed: 28442746]

McNamara A, Geng C, Turner R, Ramos-Mendez J, Perl J, Held K, Faddegon B, Paganetti H and Schuemann J 2017 Validation of the radiobiology toolkit TOPAS-nBio in simple DNA geometries Phys. Medica 33 207–15

McNamara AL. et al. 2018; Geometrical structures for radiation biology research as implemented in the TOPAS-nBio toolkit. Phys. Med. Biol. 63 :175018. [PubMed: 30088810]

Mladenov E, Magin S, Soni A and Iliakis G 2016 DNA double-strand-break repair in higher eukaryotes and its role in genomic instability and cancer: cell cycle and proliferation-dependent regulation Semin. Cancer Biol 37–38 51–64

Newpower Met al.2019Using the proton energy spectrum and microdosimetry to model proton relative biological effectivenessInt. J. Radiat. Oncol. Biol. Phys104316–24 [PubMed: 30731186]

Nygren J, Ljungman M and Ahnström M 1995 Chromatin structure and radiation-induced DNA strand breaks in human cells: soluble scavengers and DNA-bound proteins offer a better protection against single-than double-strand breaks Int. J. Radiat. Biol 68 11–8 [PubMed: 7629432]

Oeck S, Szymonowicz K, Wiel G, Krysztofiak A, Lambert J, Koska B, Iliakis G, Timmermann B and Jendrossek V 2018 Relating linear energy transfer to the formation and resolution of DNA repair foci after irradiation with equal doses of x-ray photons, plateau, or Bragg-peak protons Int. J. Mol. Sci 19 1–10

Olive PL. 1998; The role of DNA single- and double-strand breaks in cell killing by ionizing radiation. Radiat. Res. 150

Perl J, Shin J, Schumann J, Faddegon B and Paganetti H 2012 TOPAS: an innovative proton Monte Carlo platform for research Med. Phys 39 6818–37 [PubMed: 23127075]

Prise KM, Davies S and Michael BD 1987 The relationship between radiation-induced DNA double-strand breaks and cell kill in hamster V79 fibroblasts irradiated with 250 kVp x-rays, 2–3 MeV neutrons or 238 Pu alpha-particles Int. J. Radiat. Biol 52 893–902

Radulescu I, Elmroth K and Stenerlöw B 2004 Chromatin organization contributes to non-randomly distributed double-strand breaks after exposure to high-LET radiation Radiat. Res 161 1–8 [PubMed: 14680402]

Ramos-Méndez J, Perl J, Schuemann J, McNamara A, Paganetti H and Faddegon B 2018 Monte Carlo simulation of chemistry following radiolysis with TOPAS-nBio Phys. Med. Biol 63 105014 [PubMed: 29697057]

Sakata Det al.2019Evaluation of early radiation DNA damage in a fractal cell nucleus model using Geant4-DNAPhys. Medica62152–7

Schuemann J, McNamara AL, Ramos-Méndez J, Perl J, Held KD, Paganetti H, Incerti S and Faddegon B 2019 TOPAS-nBio: an extension to the TOPAS simulation toolkit for cellular and sub-cellular radiobiology Radiat. Res 191 125–38 [PubMed: 30609382]

Stewart RD, Yu VK, Georgakilas AG, Koumenis C, Park JH and Carlson DJ 2011 Effects of radiation quality and oxygen on clustered DNA lesions and cell death Radiat. Res 176 587–602 [PubMed: 21823972]

Tabata T, Ito R and Okabe S 1972 Generalized semiempirical equations for the extrapolated range of electrons Nucl. Instrum. Methods 103 85–91

Tang N, Bueno M, Meylan S, Incerti S, Tran HN, Vaurijoux A, Gruel G and Villagrasa C 2019 Influence of chromatin compaction on simulated early radiation-induced DNA damage using Geant4-DNA Med. Phys 46 1501–11 [PubMed: 30689203]

Urushibara A, Shikazono N, O'Neill P, Fujii K, Wada S and Yokoya A 2008 LET dependence of the yield of single-, double-strand breaks and base lesions in fully hydrated plasmid DNA films by 4He$_2$ + ion irradiation Int. J. Radiat. Biol 84 23–33 [PubMed: 17852554]

Ward JF1990The yield of DNA double-strand breaks produced intracellularly by ionizing radiation: a reviewInt. J. Radiat. Biol571141–50 [PubMed: 1971840]

Warmenhoven JW, Henthorn NT, Ingram SP, Chadwick AL, Sotiropoulos M, Korabel N, Fedotov S, Mackay RI, Kirkby KJ and Merchant MJ 2020 Insights into the non-homologous end joining pathway and double strand break end mobility provided by mechanistic in silico modelling DNA Repair 85 102743 [PubMed: 31759308]

Yokoya A, Shikazono N, Fujii K, Urushibara A, Akamatsu K and Watanabe R 2008 DNA damage induced by the direct effect of radiation Radiat. Phys. Chem 77 1280–5

Zhu Het al.2020Cellular response to proton irradiation: a simulation study with TOPAS-nBioRadiat. Res1949–21 [PubMed: 32401689]
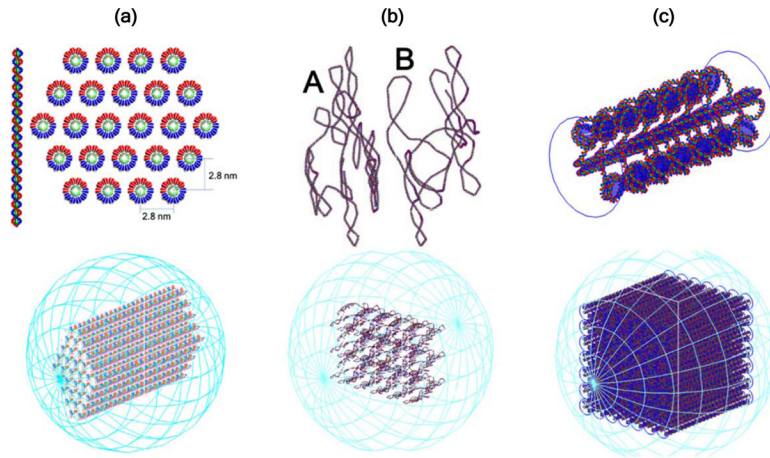
Figure 1.
Different DNA arrangements used in this work. (a) (Top) linear plasmids are straight lines as shown at left and they are arranged in a hexagonal pattern with 2.8 nm as distance between rows and columns. (Bottom) plasmids of 1286 base pair length are arranged in a 250 nm radius sphere. DNA plasmids are contained in an hexagonal prism inside the sphere with volume $V_{DNA}= 1.137\ 10^7$ nm^3. (b) (Top) single supercoiled pBR322 plasmids rolled with configurations 'A' and 'B'. (Bottom) 828 kbp of supercoiled plasmids 'A' are placed adjacent to each other in a rectangular box with volume $V_{DNA}= 1.19\ 10^8$ nm^3, while 15 kbp of plasmids 'B' are placed in a rectangular volume of $V_{DNA}= 5.3\ 10^7$ nm^3 within 500 nm radius spheres. (c) (Top) single solenoid chromatin fiber shortened for illustrative purposes. Two turns of DNA are coiled around cylindrical histones and 6 histones are placed per turn of the fiber. (Bottom) arrangement of parallel solenoid fibers in a rectangular volume of $V_{DNA}= 2.04\ 10^8$ nm^3 inside a 250 nm radius sphere. For each case, N tracks were uniformly distributed across the area σ subtended by the DNA volume, producing a fluence $\Phi = N/\sigma$.
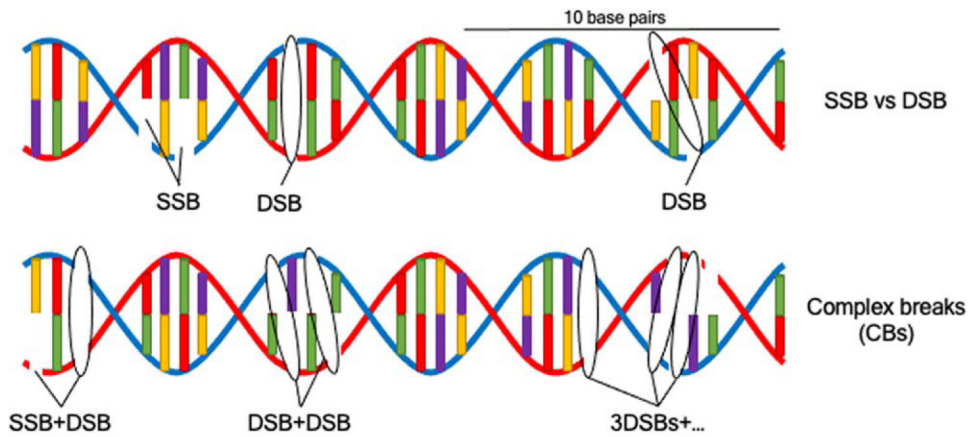
Figure 2.
Classification of damage to DNA used in this work. (Top) double strand breaks (DSBs) are defined as breaks separated by less than 10 base pairs in complementary strands. All breaks unpaired within 10 base pairs are single strand breaks (SSBs). (Bottom) complex breaks are defined as the concentration of at least one DSB plus either one or more SSB *(left)* or more than one DSB *(middle and right)* within 10 base pairs. All possible cases in complex breaks were included as a single category, being counted independently as SSBs and DSBs.
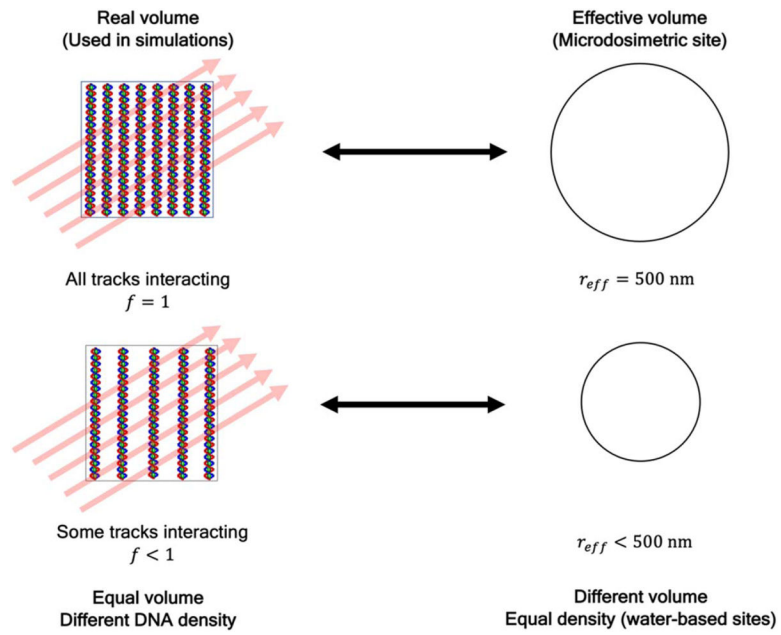
Figure 3.
Connection between our actual simulations and microdosimetric spherical sites. In real volumes filled with DNA, α-particles can cross the volumes without interacting with DNA ($f < 1$), which depends on the density of DNA, or conversely, the void space in the volume. Different DNA densities can be associated with different microdosimetric sites: the larger the density of DNA, the larger the site. The situation in which all tracks are interacting directly with DNA ($f = 1$) is arbitrarily associated with a site of 500 nm radius in this work.
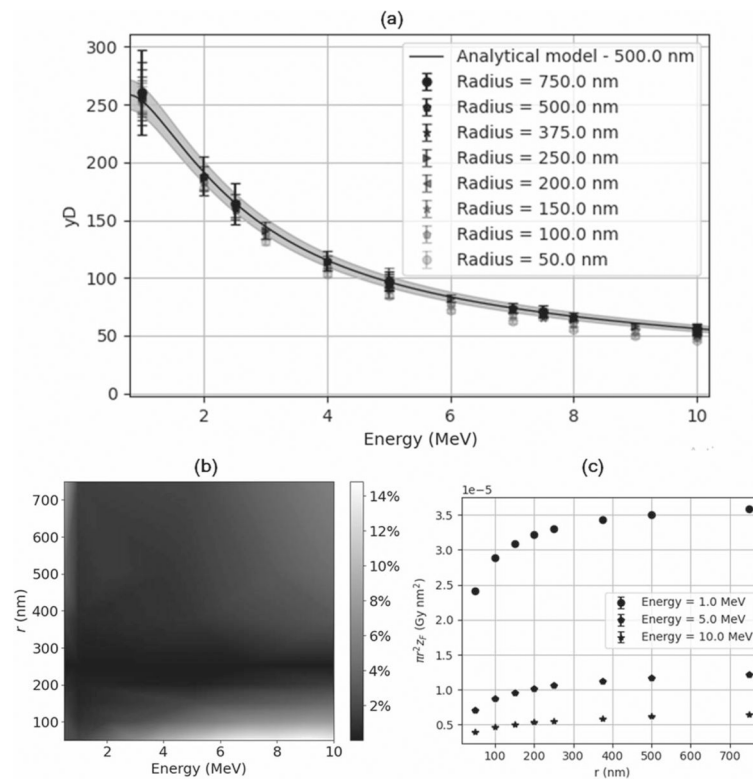
Figure 4.
(a) Points show results of y_D for monoenergetic alpha particles of 1–10 MeV from our simulations with TOPAS for several spherical sites with radii ranging from 50 to 750 nm. Error bars represent the statistical uncertainties from MC simulations. The y_D calculation using the analytical model from equations (5) and (6) for the 500 nm radius site is depicted by the solid line, while the solid band represents the 5% agreement with the analytical model. (b) 2D map of agreement of y_D to the reference site size, set at 500 nm. The gray shade bar indicates the divergence of each energy-site radius point to the reference. The map uses the results from our TOPAS simulations, and it is completed by cubic spline interpolation of these results. (c) Results of the product $\pi r^2 z_F$ for three different energies (1, 5 and 10 MeV) as a function of the site radius.
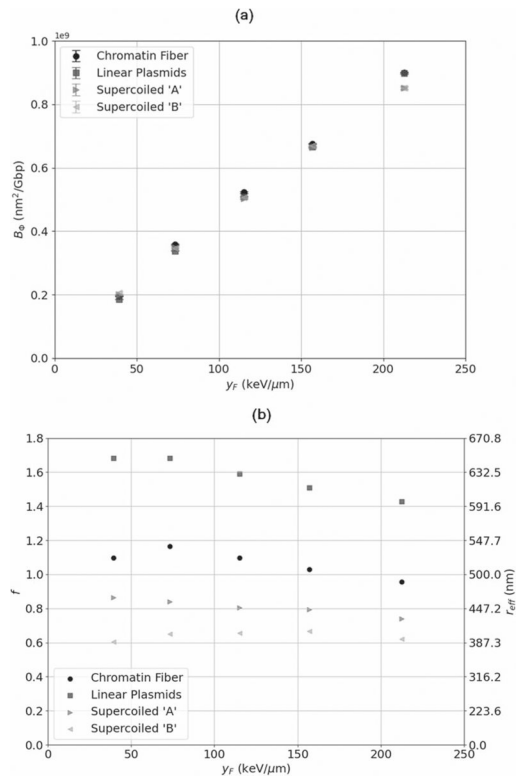
Figure 5.
(a) Total breaks produced by monoenergetic alpha particles in each of the geometries shown in figure 1 plotted as a function of y_F, calculated from the microdosimetric simulations in TOPAS. (b) Fraction of interacting tracks in each simulation and corresponding effective radius r_{eff} calculated according to equation (3).
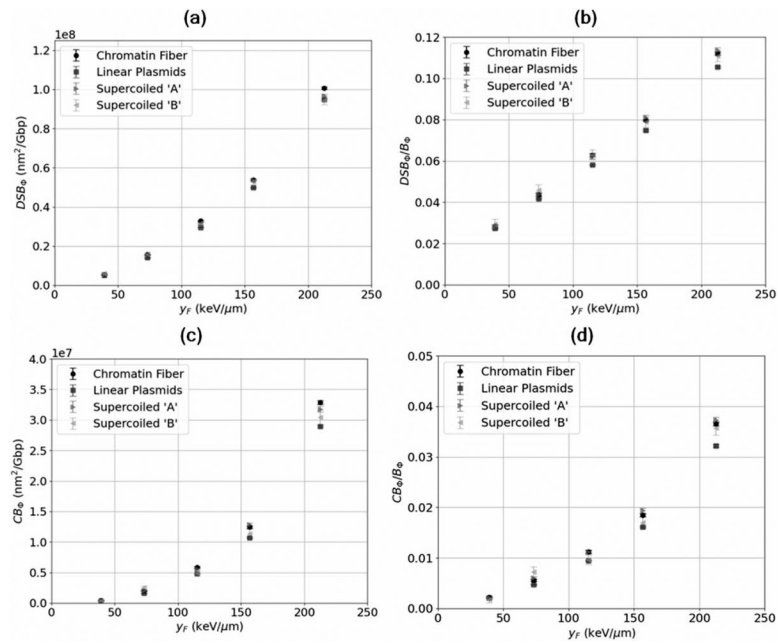
Figure 6.
Left panels show the number of DSBs (top) and CBs (bottom) per unit fluence and Gbp obtained from our TOPAS-nBio simulations for each of the geometries considered in figure 1 as a function of y_F obtained for each monoenergetic alpha particle. Right panels show the relative numbers of DSBs and CBs to the total number of breaks per track produced in each case.
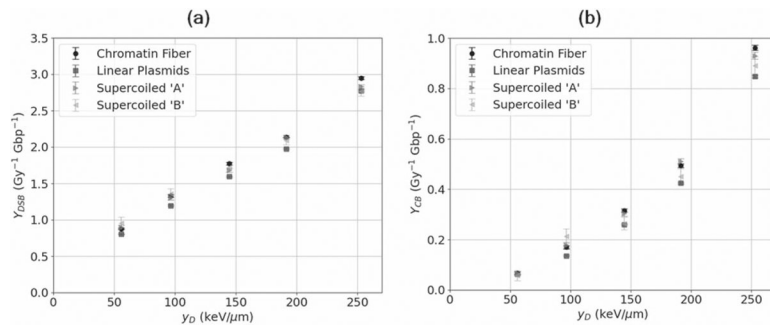
Figure 7.
Yield of (a) DSBs and (b) CBs per Gy and Gbp plotted as a function of y_D calculated for each alpha particle energy from the TOPAS-nBio simulations shown in figure 4.
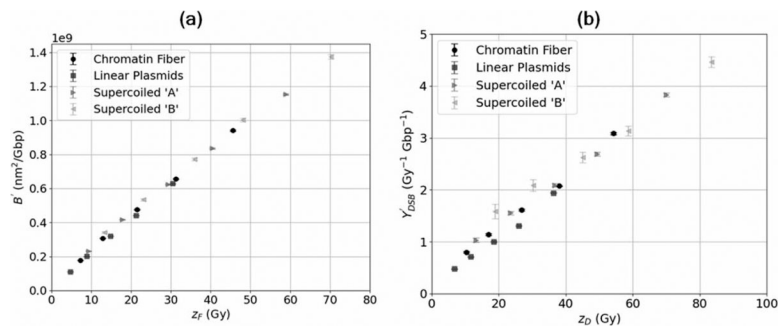
Figure 8.
(a) Total number of breaks per mass track length per Gbp; and (b) yield of DSBs per Gbp as a function of z_F using the effective radius r_{eff} as the site radius calculated with equation (3) if only tracks interacting with DNA are considered.

Table 1.

Estimation of the total number of (i) breaks per unit fluence and (ii) yield of DSB per Gbp for mixtures of chromatin fibers and supercoiled plasmids type 'A' and 'B', respectively. These estimates are compared with results from simulations of the mixtures with TOPAS-nBio. Statistical uncertainties (2σ) from these simulations are indicated for the last significant figure in each case.

					Predicted			**Results from simulations**	
Mixture	**E (MeV)**	**$z_{F_{mix}}$ (Gy)**	**$r_{eff_{mix}}$ (nm)**	**f**	**B_Φ (Gbp^{-1})**	**Y_{DSB} (Gy^{-1} Gbp^{-1})**	**f**	**B_Φ (Gbp^{-1})**	**Y_{DSB} (Gy^{-1} Gbp^{-1})**
F + ScA	1	55.6	442	0.78	1118	2.81	0.82	1171(20)	3.13(10)
F + ScA	2	38.2	458	0.84	843	2.20	0.82	866(16)	2.18(10)
F + ScA	3	27.4	464	0.86	633	1.70	0.85	650(13)	1.78(10)
F + ScA	5	16.7	474	0.90	425	1.30	0.92	453(10)	1.37(10)
F + ScA	10	8.8	478	0.91	252	0.85	0.96	254(7)	0.90(12)
F + ScB	1	64.7	410	0.67	1111	2.78	0.65	1170(42)	3.04(22)
F + ScB	2	44.3	426	0.73	842	2.17	0.65	839(34)	2.07(21)
F + ScB	3	32.7	425	0.72	624	1.67	0.69	653(27)	1.70(21)
F + ScB	5	20.8	425	0.72	413	1.18	0.69	436(20)	1.21(22)
F + ScB	10	12.0	409	0.67	239	0.75	0.69	255(14)	0.88(22)